Karya#4 Plagiasi

by Marjoni Imamora

PAPER

Check for updates

Facile charge transfer in fibrous PdPt bimetallic nanocube counter electrodes

Muhamad Adam Ramli,[a] Siti Khatijah Md Saad,[a] Elvy Rahmi Mawarnis,[b]
Marjoni Imamora Ali Umar,[c] P. Susthitha Menon,[a] Mohd Yusri Abd Rahman[a] and
Akrajas Ali Umar (ID) *[a]

The nature of the physicochemical processes and the surface reactivity of a counter electrode (CE) are determined by its surface atomic composition and area. In this paper, we investigated the role of Pd atom concentration in the electrocatalytic properties of poriferous bimetallic PdPt nanostructured CEs in dye-sensitized solar cell (DSSC) devices. It was found that the physicochemical properties and surface reactivity, which are reflected by the charge transfer resistance and electrocatalytic properties, increased with increasing Pd atom concentration and were optimum at a concentration of 2.5 mM. The DSSC device fabricated using the optimum bimetallic PdPt nanostructures produced short circuit current (J_{sc}), open circuit voltage (V_{oc}) and fill factor (FF) values as high as 9.52 mA cm^{-2}, 0.63 V and 0.37 respectively, which correspond to a power conversion efficiency (PCE) value of up to 2.22%. This is two-fold higher than the PCE of a device utilizing a pristine Pt CE (1.11%). The performance enhancement is attributed to the unique surface physicochemical properties of the prepared CE due to the poriferous structure with its large surface area and bimetallization. The synthesis and device characterization are discussed in detail.

1. Introduction

The structure, morphology and atomic composition of a counter electrode (CE) in a dye-sensitized solar cell (DSSC) device determine the redox activity for iodide/triiodide generation, charge transfer and electron conductivity in the bulk CE.[1–4] There have been continuous attempts to develop high-performance CEs in order to facilitate the above-mentioned process that range from graphene-based CEs,[5–7] to CEs based on reduced graphene oxide,[8,9] electrospun carbon,[10,11] hybrid carbon nanocomposites,[12] carbon nanofiber–TiO$_2$ nanoparticle composites,[13] AgGeS alloys[14] and Ag–AgSnS heterojunctions.[15] Nevertheless, CEs with large surface areas and high densities of active sites facilitate dynamic electrocatalytic processes at the electrolyte/CE interface.[5,7,10,16] Thus, CEs with porous and fibrous morphology may promise the efficient diffusion of redox species, so accelerating electrocatalytic charge transfer.[13,14,17,18] In many cases, electrocatalytic processes on the CE are limited by active site poisoning from the redox species residue, deteriorating the overall redox activity on the surface.

The introduction of foreign ions into a host CE to form a bimetallic system modifies the surface electronic density of states *via* d-orbital mixing and surface strain and reconstruction, so modulating the catalytic performance of the CE.[19–21] This may promote highly dynamic redox reactions on the surface, suppressing the active site poisoning.

Bimetallic nanostructures with high porosities and fibrous morphologies have been prepared *via* a large range of methods, including the reduction of metal precursors by oxygen plasma,[22] the dry plasma reduction of metal precursors,[23] electrochemical deposition,[24] *etc.* We recently developed a straightforward approach for the direct growth of a metal or bimetal system on a solid substrate *via* a liquid phase deposition (LPD) method. By simply reducing the metal precursor using formic acid in the presence of surfactant, fibrous metal or bimetal nanostructures with morphologies ranging from spherical to cubic, and hierarchical structures were successfully produced.[25–27]

Here we report an enhancement in charge transfer activity in a DSSC device by utilizing a PdPt fibrous nanocube CE and a photoanode made from anatase TiO$_2$ nanowalls.[28–30] In a typical process, we found that the charge transfer characteristics were strongly influenced by the atomic composition of the PdPt, and we optimized the PdPt concentration ratio at 2.5 : 10 on the basis of electrochemical impedance spectroscopy (EIS) and cyclic voltammetry (CV) studies. In the optimum conditions, a charge transfer resistance (R_{ct}) as low as 0.5 Ω was obtained.

[a] *Institute of Microengineering and Nanoelectronics, Universiti Kebangsaan Malaysia, 43600, Bangi, Selangor, Malaysia. E-mail: akrajas@ukm.edu.my; Fax: +603 8925 0439; Tel: +603 8911 8547*

[b] *Department of Chemistry Education, Faculty of Tarbiyah, Institut Agama Islam Negeri (IAIN), 27213 Batusangkar, West Sumatera, Indonesia*

[c] *Department of Physics Education, Faculty of Tarbiyah, Institut Agama Islam Negeri (IAIN), 27213 Batusangkar, West Sumatera, Indonesia*

This special charge transfer performance promoted an efficient photovoltaic process in the device, improving photogenerated current transport and photon-to-current conversion efficiency. A power conversion efficiency (PCE) as high as 2.22% was obtained in this study.

2. Experimental

2.1 Preparation of PdPt FNC CEs

PdPt fibrous nanocrystals (FNCs) were prepared using our recently reported approach, namely LPD.[25–27,31] In a typical process, cleaned fluorine-doped tin oxide (FTO) substrates were simply immersed in a 15 mL growth solution that contained 15 mM potassium hexachloroplatinate(IV), 10 mM sodium dodecyl sulfate, 5 mM formic acid and potassium hexachloropalladate(IV). The concentration of palladium from the precursor of potassium hexachloropalladate was varied from 0.5 to 3.0 mM. The growth solution was stirred on a hotplate at 400 rpm at 40 °C for 7 h. A uniform grey black film was obtained on the substrate surface every time after completing the growth process. After that, the samples were taken out and washed with copious amounts of water and then dried in an electrical oven at 100 °C for 10 min. All chemicals were purchased from Sigma-Aldrich and used directly without any further purification, and all solutions were prepared using deionized water obtained from a Milli-Q water purification system.

2.2 Preparation of TiO₂ nanowall photoanode

The TiO$_2$ nanowall photoanode was prepared using our previously reported method,[28,32–35] namely LPD with modifications.[36–38] Briefly, the preparation process was as follows: firstly, a cleaned indium tin oxide (ITO) substrate was immersed in a solution containing 5 mL of 0.5 M ammonium hexafluorotitanate, $(NH_4)_2TiF_6$, and 2 mL of 0.5 M hexamethylenetetramine (HMT). The reaction was then performed in a water bath for 5 h at 90 °C. The sample was taken out, washed with deionized water and dried in an electrical oven at 100 °C for 10 minutes. The sample was then annealed at 450 °C for about 4 h. All chemicals were purchased from Sigma-Aldrich and used as received.

2.2 Characterization

The morphologies of the PdPt FNCs were characterized using field-emission scanning electron microscopy (FESEM; Zeiss Supra 55VP FESEM model with a resolution of 1.0 nm at 30 kV). The elemental compositions of the samples were characterized using energy dispersive spectroscopy (EDS) obtained using an FESEM apparatus equipped with an energy dispersive X-ray (EDX) analysis tool. Meanwhile, structural analysis was performed by X-ray diffraction spectroscopy (XRD) using a Bruker D8 system with Cu Kα irradiation ($\lambda = 1.541$ Å) and a scan rate of 20° min^{-1}.

2.3 Electrocatalytic properties

The electrocatalytic activities of the PdPt FNC CEs were studied via a three-electrode system using a Gamry 1000 interface. CV experiments were carried out in an electrolyte containing 50 mM LiI, 10 mM I$_2$ and 0.5 M LiClO$_4$ in acetonitrile. A scan rate of 50 mV s^{-1} with a potential window of −0.6 to 1.2 V was used. Ag/AgCl saturated in 2.0 M KCl was used as the reference electrode.

2.4 DSSC fabrication and characterization

A DSSC device with the structure ITO/photoanode/N719/electrolyte/PdPt was fabricated to evaluate the role of PtPd as the CE in the device performance. TiO$_2$ nanowalls were prepared using our previously reported method, and were used as the photoanode. Prior to the device fabrication, the TiO$_2$ photoanode was immersed in an ethanolic solution of 0.05 mM N719 dye (Sigma-Aldrich, USA) for 15 h at room temperature. The DSSC device was then fabricated by assembling the photoanode and PdPt together using metal clamps. A parafilm with a thickness of 2 mm and a circle hole with an area of 0.23 cm^2 were sandwiched between the photoanode and PdPt CE. The EL-HPE high performance electrolyte from Dyesol (Australia) was then injected into the hole.

The photocurrent (J–V) response of the DSSC was examined using a Gamry 1000 potentiostat under illumination by simulated solar light (AM1.5) with an intensity of 100 mW cm^{-2} (Newport LC-100 150 W). The charge transfer characteristics of the device were evaluated using EIS. The incident photon-to-current conversion efficiency (IPCE) was examined using the PVE 300 photovoltaic EQE and IQE solution system (Bentham, UK) using a 75 W Xenon light and a 100 W Quartz halogen light as the light sources. The IPCE tests were done in the wavelength range of 300–800 nm.

3. Results and discussion

3.1 PdPt morphology properties

We have successfully deposited fibrous PdPt FNCs directly onto an FTO substrate using the present approach. FESEM analysis results show that the nanostructures efficiently cover the entire substrate surface (Fig. 1A). As can be seen from Fig. 1A–E, the nanostructures mainly display the morphologies of cubic and truncated cubic-like structures. Their dimensions range from approximately 60 to 100 nm and their yield is as high as 70%. The remaining products are irregular shaped structures with dimensions that are relatively higher than those of the main cubic-like structures, extending up to 200 nm. Interestingly, all of the nanostructured products are actually fibrous structures as clearly indicated by the existence of hairy entities on the surface of the products. TEM analysis (Fig. 1F and G) further verifies the fibrous nature of the PdPt nanocubes which are constructed of interconnected nanowires with lengths and diameters of approximately 40 and 10 nm, respectively. The fibrous nanowires have aligned themselves and formed mixed structures between perfect cubes (Fig. 1C) and rounder structures (Fig. 1B) with dimensions of about 60 nm. Such unique fibrous structures promise high surface areas that offer the potential for surface activity such as charge transfer and redox reactions.[25–27,31,39] They should also enhance surface reactions and accelerate the catalytic processes at the surface of the sample. Thus, it is expected that the fibrous PdPt nanocubes will have potential as a high-performance CE in DSSC devices.
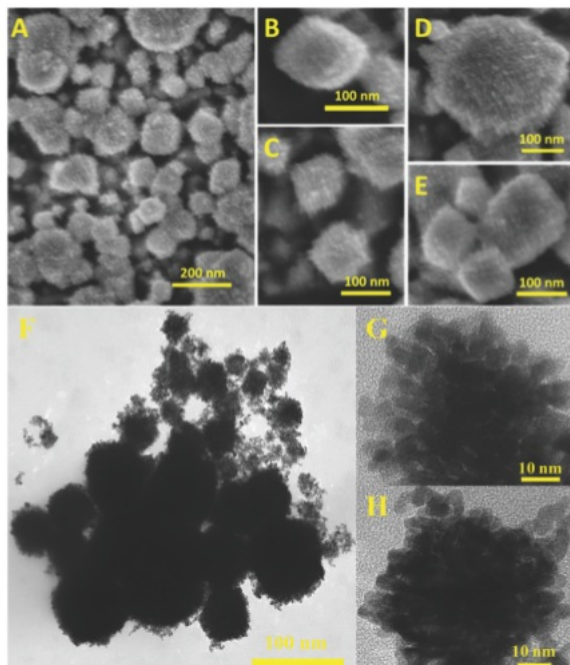
Fig. 1 (A–E) Typical FESEM images of the optimum PdPt FNCs (Pd concentration of 2.0 mM). (F–H) Low- and high-resolution TEM images of PdPt FNCs.

Fig. 2A shows a typical XRD spectrum for the PdPt nanostructures on the FTO substrate. As can be seen from Fig. 2, typical diffraction peaks at 40.11, 46.64, 68.10, 82.08 and 86.60° are observed. These peaks correspond to the (111), (200), (220), (311) and (222) planes of PdPt.[40] These five peaks seem to match with Pd and Pt diffraction peaks, but, according to the magnified spectra shown in Fig. 2B, they are slightly shifted from the individual Bragg planes, implying the effective formation of a bimetallic compound as the Pd ions are introduced into the Pt host lattices.[25–27,41] The table inset in Fig. 2 shows a comparison between the diffraction peak positions of the PdPt bimetal and the individual peaks of Pt and Pd. As observed from the tables, the two main peaks of the (111) and (200) planes shift to higher angles in the PdPt bimetal by about 0.68 and 0.55° with respect to Pt and by about 2.06 and 1.63° with respect to Pd. In contrast, the (220) peak for the bimetal lies in between the individual peaks of Pt and Pd. The different shifting directions for particular Bragg planes relative to the diffraction spectrum of the Pt host upon bimetallization with Pd indicate the co-presence of stress and strain in the lattices. This may lead to a modification of the electron cloud distribution at particular Bragg planes, improving the surface activity of the bimetal and promoting a superior catalytic property for a CE in DSSCs.[25,42]

2.1 Photovoltaic performances

Fig. 3 shows J–V curves of DSSC devices utilizing PdPt CEs prepared with different concentrations of Pd atoms. As revealed
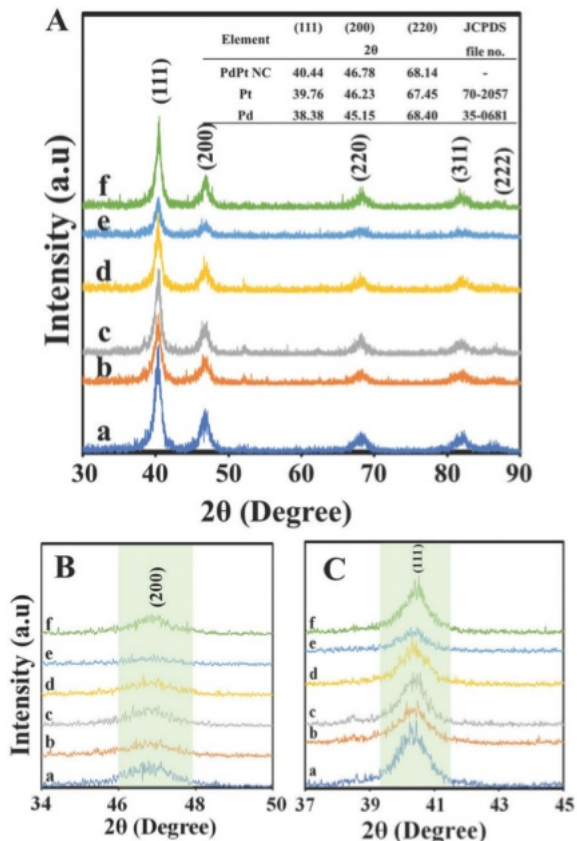

Fig. 2 (A) XRD spectra of PdPt samples with different concentrations of Pd atoms, namely 0.5 (a), 1.0 (b), 1.5 (c), 2.0 (d), 2.5 (e) and 3.0 mM (f). (B and C) Magnified spectra for the (111) and (200) Bragg planes, respectively. The inset table in (A) shows the peak positions of the main Bragg planes of PdPt and their comparison to the peaks for the individual Pt and Pd.
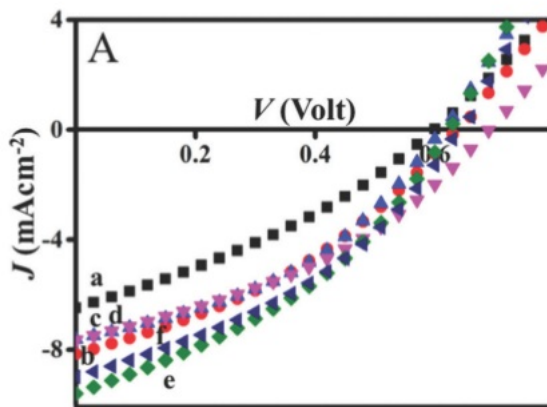

Fig. 3 J–V curves of DSSCs utilizing PdPt FNC CEs with different concentrations of Pd, namely 0.5 (a), 1.0 (b), 1.5 (c), 2.0 (d), 2.5 (e) and 3.0 mM (f), under solar light illumination (AM1.5) at 100 mW cm^{-2}.

from Fig. 3A and the summary of DSSC parameters in Table 1, the short circuit current (J_{sc}) under simulated solar light

Table 1 Photovoltaic and electrochemical parameters of DSSCs utilizing PdPt FNC CEs with different Pd ion concentrations

Pd ions (mM)	0.5	1.0	1.5	2.0	2.5	3.0
Photovoltaic parameter						
J_{sc} (mA cm^{-2})	6.47 ± 0.18	7.57 ± 0.42	7.60 ± 0.64	8.10 ± 0.46	9.52 ± 0.23	8.92 ± 0.02
V_{oc} (V)	0.62 ± 0.00	0.64 ± 0.00	0.62 ± 0.01	0.70 ± 0.00	0.63 ± 0.00	0.64 ± 0.00
Efficiency (%)	1.26 ± 0.08	1.86 ± 0.07	1.88 ± 0.06	1.96 ± 0.06	2.22 ± 0.07	2.17 ± 0.07
FF	0.31 ± 0.00	0.36 ± 0.00	0.40 ± 0.01	0.37 ± 0.00	0.37 ± 0.01	0.38 ± 0.00
Lifetime (ms)	86.43	91.74	100.27	116.48	125.44	122.40
Electrochemical parameter						
E_{red1} (V)	0.23	0.21	0.23	0.30	0.25	0.22
J_{red1} (mA cm^{-2})	8.49	3.91	6.12	7.53	8.54	7.64
E_{ox1} (V)	0.77	0.74	0.74	0.78	0.75	0.76
E_{pp} (V)	0.54	0.53	0.52	0.48	0.49	0.54
R_{ct1} (Ω)	6.2	4.8	2.2	1.50	0.5	1.08
R_{ct2} (Ω)	19.8	17	16	15	13.4	14

illumination increases with increasing Pd atom concentration and is optimum at a concentration of 2.5 mM. In other words, J_{sc} changes from 6.57 to 9.52 mA cm^{-2} when the concentration of Pd is increased from 0.5 to 2.5 mM. The J_{sc} value reduces as the concentration of Pd atoms exceeds the optimum concentration. As seen in Table 1, the open circuit voltage (V_{oc}) values all fall in a small range, *i.e.* 0.63 to 0.70 V. This could be because the devices have similar characteristics due to their identical TiO$_2$ nanowall photoanodes. The fill factor (FF), similar to V_{oc}, does not change as the Pd concentration in the CE is varied. We calculated the PCE of the devices and it was found that these improved from 1.26% for the CE with the lowest Pd concentration to 2.22% for the optimum CE.

These phenomena may be explained using the following reasons. Firstly, electrocatalytic properties are improved upon bimetallization. As revealed from the CV results in Fig. 4, the CEs demonstrate excellent electrocatalytic properties by exhibiting a pair of reduction and oxidation peaks corresponding to the I^-/I_3^- redox species (*i.e.*, 0.20 and 0.77 V for the reduction and oxidation peaks, respectively).[24] Even though the oxidation of triiodide (I_3^-) is undetermined in this work, our findings are in good agreement with those in a previous study reported by another group.[24] We expect that the lack of oxidation of triiodide is due to the fact that our CE is dominated by the presence of Pt atoms whose work function is critically un-matched with the triiodide redox potential. It could also be caused by the existence of residual chloride ions on the surface of the CEs formed during the synthetic process which utilizes the PtCl$_6^-$ precursor. These could hamper the oxidation of triiodide species. The enhancement of the electrocatalytic properties of the CEs can also be observed from the improvement in the current density of reduction (J_{red}) and peak-to-peak separation (E_{pp}) values. As presented in Fig. 4, the J_{red} increases with increasing Pd atom concentration in the CE, while E_{pp} decreases with increasing Pd atom concentration, confirming the enhancement of the electrocatalytic properties of the CEs upon bimetallization. These will improve the PCE. It is true that the lowest Pd concentration also presents a high J_{red} (see Table 1). However, the E_{pp} of this CE is also high, showing that the sample features relatively poor electrocatalytic properties. The improvement of the electrocatalytic properties of the CE can simply be attributed to the presence of Pd
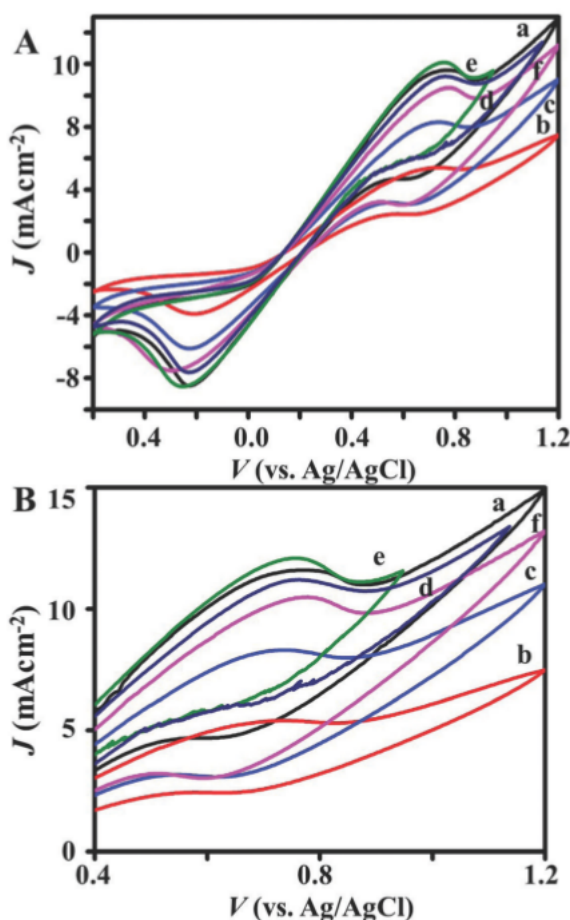

Fig. 4 (A) CV curves of PdPt FNCs samples with different Pd concentrations, namely 0.5 (a), 1.0 (b), 1.5 (c), 2.0 (d), 2.5 (e) and 3.0 mM (f), in an electrochemical cell containing I^-/I_3^- electrolyte at room temperature and at a scan rate of 50 mV s^{-1}. (B) Magnified spectra for the potential window of 0.4 to 1.2 V.

in the Pt lattices which may offer better surface physicochemical properties.[43]

To further verify the electrocatalytic activity of the CE, we carried out Tafel polarization analysis. The results are shown
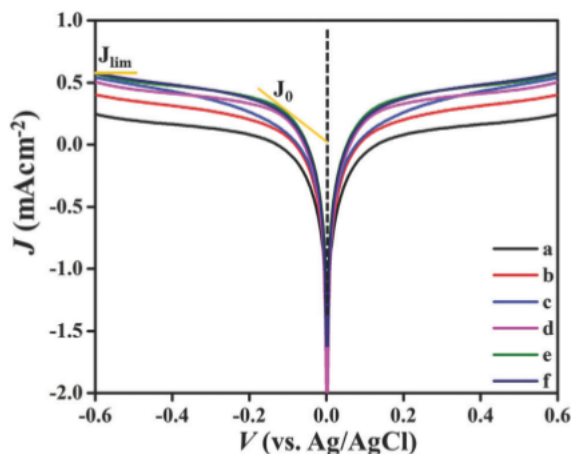
Fig. 5 Tafel polarization plots of the PdPt CEs with different Pd concentrations, namely 0.5 (a), 1.0 (b), 1.5 (c), 2.0 (d), 2.5 (e) and 3.0 mM (f).

Fig. 6 (A) EIS and (B) the typical curve fitting profile of the EIS result following the equivalent circuit given in the inset to A. (C) Bode plots for DSSC device utilizing PdPt FNCs as the CE at different Pd concentrations, namely 0.5 (a), 1.0 (b), 1.5 (c), 2.0 (d), 2.5 (e) and 3.0 mM (f).

in Fig. 5. As Fig. 5 reveals, the anodic and cathodic currents increase as the Pd concentration increases in the PdPt CE and are maximum for the optimum CE (sample c). From the curve, we can deduce the exchange current density (J_o) and the limiting current density (J_{lim}), which respectively represent the electrocatalytic activity and the diffusion characteristics of the redox couple over the CEs. The current density at the intersection of the tangential line to the offset potential region on the cathodic polarization zone with the Tafel zone line gives J_o (see Fig. 5) and the saturated current density is J_{lim}.[44] It is found that the optimum sample shows the highest J_o and J_{lim} values suggesting its superior electrocatalytic activity for the reduction of I_3^- ions. This phenomenon will certainly drive diffusion of the active redox couple I^-/I_3^- in the electrolyte. These results are consistent with the EIS result shown in Fig. 6 as the J_o and J_{lim} values are inversely proportional to the R_{ct} and the Nernst diffusion resistance.

In addition, there is an enhanced charge transfer process in the bimetallic CE. As judged from the EIS analysis results shown in Fig. 6A, which are well-fitted with the equivalent circuit shown in the inset of Fig. 6A (see the fitted result in Fig. 6B), the interfacial charge transfer characteristic of the CE is increased by modifying the concentration of Pd in the CE. According to the analysis, it is inferred that the optimum CE (curve e) has the lowest charge transfer resistance (R_{ct1}), which is represented by the small diameter of the first semicircle in the high frequency region. Because the semicircle is also influenced by the constant phase element 1 (CPE1), which is low in value, it is further verified that the CE enables facile charge collection and transport as it features a relatively low capacitance due to limited charge accumulation at the CE interface. Interestingly, the enhancement in the charge transfer characteristic of the CE also effectively drives an active charge transfer dynamic at the TiO$_2$ nanowire (TNW)–dye/electrolyte interfaces and redox species diffusion in the electrolyte, as suggested by the significantly low value of Nernst diffusion
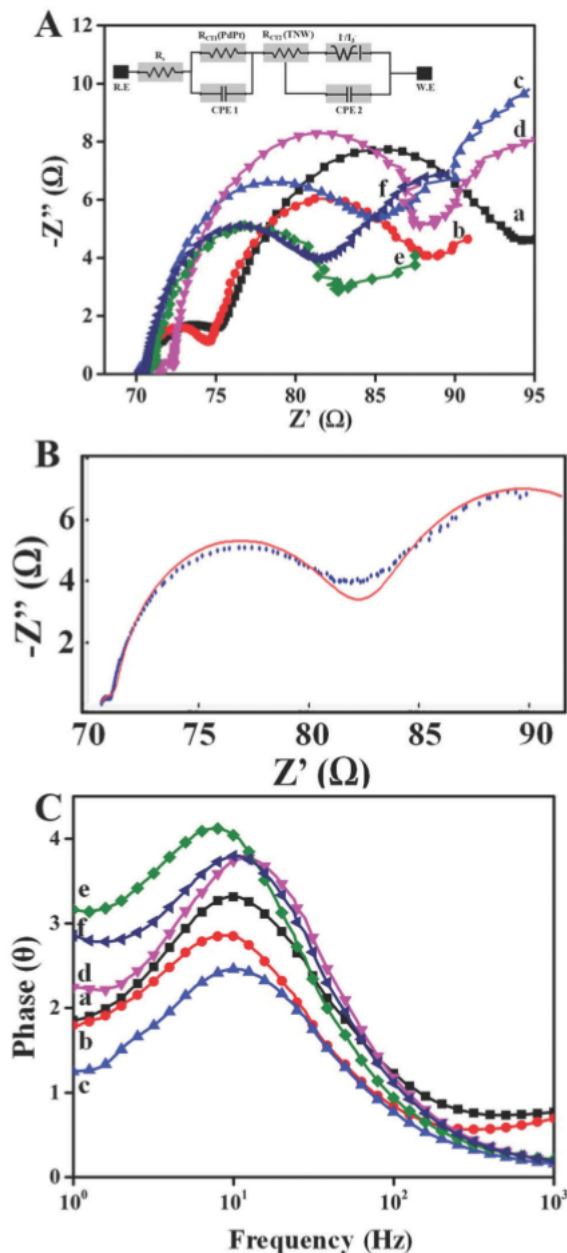
impedance (Z_w) of the electrolyte. These conclusions are indicated by the relatively low diameter of the semicircle in the middle frequency region of the spectrum (representing R_{ct2} and CPE2) and the semicircle in the low frequency region (corresponding to the Warburg element in the equivalent circuit). The phenomena are also supported by the CV results, which convey a large faradaic current and small E_{pp}.
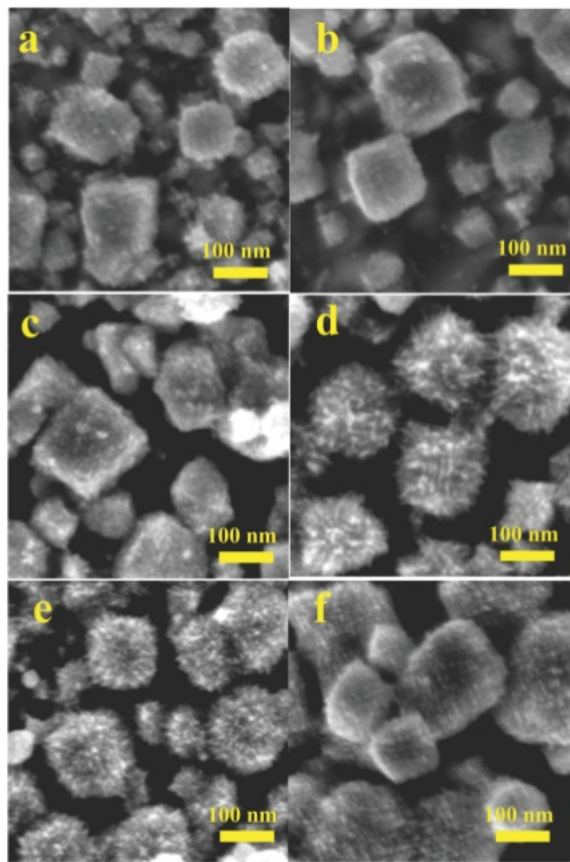
Fig. 7 Typical FESEM images of PdPt FNCs at different Pd atom concentrations, namely 0.5 (a), 1.0 (b), 1.5 (c), 2.0 (d), 2.5 (e) and 3.0 mM (f).

Fig. 8 J–V curves in dark conditions from DSSC devices utilizing PdPt FNCs with different Pd concentrations, namely 0.5 (a), 1.0 (b), 1.5 (c), 2.0 (d), 2.5 (e) and 3.0 mM (f).

Moreover, the CE has a large surface area due to its fibrous structure. As mentioned earlier, the PdPt FNCs have a poriferous structure that is constructed from a fiber network. This provides a large surface area for facile electrolyte diffusion,[45] facilitating an active physicochemical process on the surface. As can be seen from Fig. 7, the optimum sample has the greatest number of anchoring fibers protruding from the cubic structure, enhancing the electrocatalytic process. In addition, the optimum sample has slightly smaller fibers that may produce a structure with a higher surface energy. This condition may accelerate both the electron transfer kinetics and I_3^- reduction reaction.

Thus, owing to the existence of the above-mentioned phenomena, the carrier transfer at the electrolyte/CE interface and the transport in the device become progressive and facile, and in turn promote a long carrier lifetime,[46] enhanced quantum capacitance[47] and limited recombination at the interface.[48] The initial phenomenon is confirmed by the Bode plot results (Fig. 6C) and dark current analysis (Fig. 8). As expected, according to the Bode plot analysis result, the carrier lifetime of the optimum sample is as high as 125.44 ms, which is relatively higher than those of the other PdPt samples (see Table 1). It can also be seen that the optimum sample shows
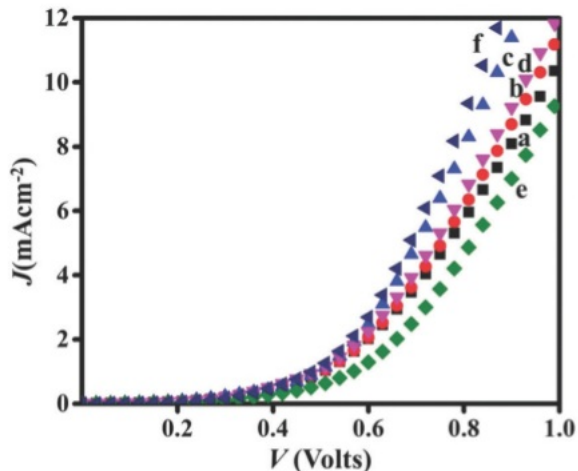
the maximum frequency shift to the lower frequency region, reflecting the high diffusion rate of electrolyte on the surface of the CE, which augments the interfacial charge transfer at the electrolyte/CE interface. Meanwhile, the limited electron–hole recombination is verified by the relatively higher threshold voltage of the J–V curve in the dark (see Fig. 8). As can be seen from Fig. 8, the optimum sample exhibits a much higher threshold voltage than the other samples, implying a limited photogenerated carrier recombination. It is true that the carrier recombination process largely occurs in the semiconducting photoanode system. However, a positive carrier injection (forward charge transfer process) at the electrolyte/CE interface is required to drive effective carrier transportation and separation *via* the build-up of high electrical potential difference across the device. Thus, CEs with low charge transfer resistances are necessary.[44,49–52]

It is true that, even though an enhanced carrier dynamic is observed at the electrolyte/CE interface when utilizing PdPt FNCs, the overall performance is still relatively low. This could be directly related to the nature of the carrier dynamic at the electrolyte/TiO$_2$–dye interface. We carried out an external quantum efficiency analysis on the optimum device to verify the nature of carrier extraction to the electrode and the spectral sensitivity of the DSSC utilizing the PdPt FNC CE. The result is shown in Fig. 9. As the result reveals, the device actually shows quite a wide spectral sensitivity, *i.e.*, a wavelength window of 450 to 600 nm, which is comparable to that of another recently reported DSSC device,[53] as well as a maximum IPCE value of 35.5%. This value is well in accordance with the current density in the J–V curve and the PCE value of 2.22%. Thus, from this IPCE analysis result and on the basis of the CE properties obtained in this study, it is clear that the nature of the carrier dynamic at the electrolyte/TiO$_2$–dye interface is the most likely factor for the deficiency in the overall performance. High-performance DSSC devices should
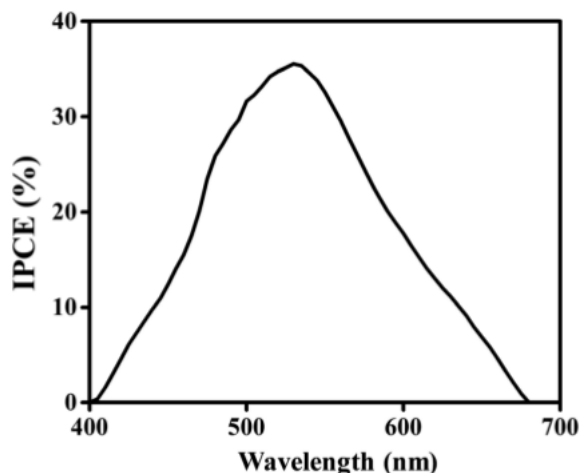
Fig. 9 The IPCE spectrum of a DSSC device utilizing the optimum PdPt FNC CE (0.25 mM Pd).

be obtained when the interfacial carrier dynamic in the device is optimized.

While the analysis results explicitly suggest that the new CE features an interesting electrocatalytic activity, we analyzed the stability properties of the CE by evaluating its CV response under repeated use while aged in an ambient atmosphere for up to 15 days. The results are shown in Fig. 10. As can be seen from the figure, the CE is relatively stable for repeated use (twice for 5 days) with an initial decrease in the J_{sc} value of as little as 10% of the initial value and then a gradual decrease with further re-use and aging. Nevertheless, judging from the results, the positions of the potential reduction (E_{red1}) and potential oxidation (E_{ox1}) are relatively unchanged over repeated use (15 days of evaluation), which indicates the persistence of the electrocatalytic properties of the CE.
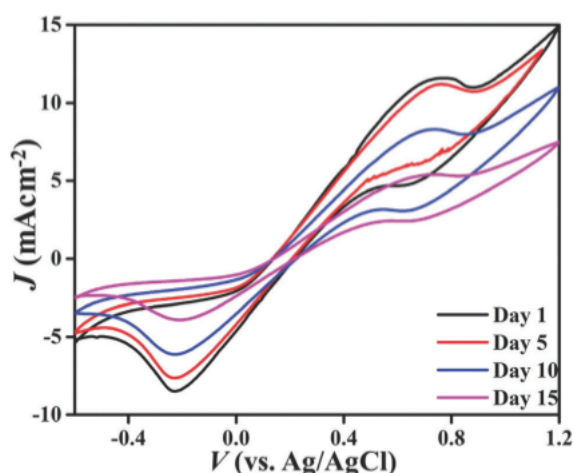

Fig. 10 CV profiles of the device utilizing the optimum CE measured repeatedly over 15 days.

4. Conclusion

The role of the Pd atom concentration in poriferous bimetallic PdPt FNC CEs in the performance of DSSCs has been investigated. It was found that the performance of DSSCs increases with increasing Pd atom concentration in the bimetallic PdPt FNC CE. The optimum concentration was found to be 0.25 mM. At this condition, J_{sc}, V_{oc} and FF values as high as 9.52 mA cm^{-2}, 0.63 V and 0.37 respectively, were achieved. These give an equivalent PCE value of as high as 2.22%. This performance represents a two-fold improvement when compared to that of the pristine Pt CE (1.11%). The existence of a poriferous structure provides a large surface area, and the special surface physicochemical properties due to the bimetallization process promote facile charge transfer and active electrocatalytic properties. These are considered to be the key factors in the improvement of the PCE. The present performance is still marginal when put in the context of recent reports, due to the device construction and electrolyte stability issue. However, the present results provide a strategic alternative for achieving high performance DSSC devices. High performance DSSCs may be obtained using this CE when the critical issues are solved.

Conflicts of interest

There are no conflicts of interest to declare.

Acknowledgements

References

1 M. Chen and D. Goodman, Structure–activity relationships in supported Au catalysts, *Catal. Today*, 2006, **111**(1–2), 22–33.

2 G. Inoue and M. Kawase, Numerical and experimental evaluation of the relationship between porous electrode structure and effective conductivity of ions and electrons in lithium-ion batteries, *J. Power Sources*, 2017, **342**, 476–488.

3 S. Shan, *et al.*, Catalytic activity of bimetallic catalysts highly sensitive to the atomic composition and phase structure at the nanoscale, *Nanoscale*, 2015, **7**(45), 18936–18948.

4 V. R. Stamenkovic, *et al.*, Trends in electrocatalysis on extended and nanoscale Pt-bimetallic alloy surfaces, *Nat. Mater.*, 2007, **6**(3), 241.

5 J. Gong, *et al.*, Activated graphene nanoplatelets as a counter electrode for dye-sensitized solar cells, *J. Appl. Phys.*, 2016, **119**(13), 135501.

6 U. Mehmood, Efficient and economical dye-sensitized solar cells based on graphene/TiO$_2$ nanocomposite as a photoanode

and graphene as a Pt-free catalyst for counter electrode, *Org. Electron.*, 2017, **42**, 187–193.

7 Z. Zhou, *et al.*, Graphene-beaded carbon nanofibers with incorporated Ni nanoparticles as efficient counter-electrode for dye-sensitized solar cells, *Nano Energy*, 2016, **22**, 558–563.

8 N. Mustaffa, M. Y. A. Rahman and A. Umar, Dye-sensitized solar cell utilizing silver-reduced graphene oxide film counter electrode: effect of silver content on its performance, *Ionics*, 2018, **24**(11), 3665–3671.

9 M. Rahman, A. Sulaiman and A. Umar, Dye-sensitized Solar Cell utilizing Gold Doped Reduced Graphene Oxide Films Counter Electrode, *J. New Mater. Electrochem. Syst.*, 2018, **21**(2), 113–117.

10 X. Ma, *et al.*, Electrospun carbon nano-felt derived from alkali lignin for cost-effective counter electrodes of dye-sensitized solar cells, *RSC Adv.*, 2016, **6**(14), 11481–11487.

11 A. Aboagye, *et al.*, Electrospun carbon nanofibers with surface-attached platinum nanoparticles as cost-effective and efficient counter electrode for dye-sensitized solar cells, *Nano Energy*, 2015, **11**, 550–556.

12 Q. Chang, *et al.*, *In situ* Grown Hybrid Nanocarbon Composite for Dye Sensitized Solar Cells, *Electrochim. Acta*, 2015, **166**, 134–141.

13 S. Sigdel, *et al.*, Dye-sensitized solar cells based on spray-coated carbon nanofiber/TiO₂ nanoparticle composite counter electrodes, *J. Mater. Chem. A*, 2014, **2**(29), 11448–11453.

14 Q. He, *et al.*, Efficient Ag₈GeS₆ counter electrode prepared from nanocrystal ink for dye-sensitized solar cells, *J. Mater. Chem. A*, 2015, **3**(40), 20359–20365.

15 Q. He, *et al.*, The Role of Mott–Schottky Heterojunctions in Ag–Ag₈SnS₆ as Counter Electrodes in Dye-Sensitized Solar Cells, *ChemSusChem*, 2015, **8**(5), 817–820.

16 H. Cui, *et al.*, N-Doped graphene frameworks with super-high surface area: excellent electrocatalytic performance for oxygen reduction, *Nanoscale*, 2016, **8**(5), 2795–2803.

17 Q. Lu, *et al.*, Highly porous non-precious bimetallic electrocatalysts for efficient hydrogen evolution, *Nat. Commun.*, 2015, **6**, 6567.

18 A. Iefanova, *et al.*, Transparent platinum counter electrode for efficient semi-transparent dye-sensitized solar cells, *Thin Solid Films*, 2014, **562**, 578–584.

19 K.-H. Bae, *et al.*, PtZn nanoalloy counter electrodes as a new avenue for highly efficient dye-sensitized solar cells, *J. Alloys Compd.*, 2017, **702**, 449–457.

20 H. Cai, *et al.*, PtRu nanofiber alloy counter electrodes for dye-sensitized solar cells, *J. Power Sources*, 2014, **258**, 117–121.

21 J.-S. Kim, *et al.*, Optimum alloying of bimetallic PtAu nanoparticles used as an efficient and robust counter electrode material of dye-sensitized solar cells, *J. Alloys Compd.*, 2016, **682**, 706–712.

22 O. Omelianovych, *et al.*, Characterization of surface chemistry of PtFe bimetallic nanoparticles, *Appl. Surf. Sci.*, 2018, **457**, 381–387.

23 V.-D. Dao, *et al.*, Efficiency Enhancement of Dye-Sensitized Solar Cell Using Pt Hollow Sphere Counter Electrode, *J. Phys. Chem. C*, 2011, **115**(51), 25529–25534.

24 Q. Yang, *et al.*, Ternary platinum alloy counter electrodes for high-efficiency dye-sensitized solar cells, *Electrochim. Acta*, 2016, **190**, 85–91.

25 E. R. Mawarnis, *et al.*, Hierarchical Bimetallic AgPt Nanoferns as High-Performance Catalysts for Selective Acetone Hydrogenation to Isopropanol, *ACS Omega*, 2018, **3**(9), 11526–11536.

26 E. Rahmi, *et al.*, Fibrous AuPt bimetallic nanocatalyst with enhanced catalytic performance, *RSC Adv.*, 2016, **6**(33), 27696–27705.

27 A. A. Umar, *et al.*, Highly-reactive AgPt nanofern composed of {001}-faceted nanopyramidal spikes for enhanced heterogeneous photocatalysis application, *J. Mater. Chem. A*, 2014, **2**(41), 17655–17665.

28 S. K. Md Saad, *et al.*, Two-Dimensional, Hierarchical Ag-Doped TiO₂ Nanocatalysts: Effect of the Metal Oxidation State on the Photocatalytic Properties, *ACS Omega*, 2018, **3**(3), 2579–2587.

29 S. K. Md Saad, *et al.*, Porous(001)-faceted Zn-doped anatase TiO₂ nanowalls and their heterogeneous photocatalytic characterization, *RSC Adv.*, 2014, **4**(100), 57054–57063.

30 S. K. M. Saad, *et al.*, Porous Zn-doped TiO₂ nanowall photoanode: effect of Zn²⁺ concentration on the dye-sensitized solar cell performance, *Appl. Surf. Sci.*, 2015, **353**, 835–842.

31 A. Balouch, *et al.*, Fibrous, ultra-small nanorod-constructed platinum nanocubes directly grown on the ITO substrate and their heterogeneous catalysis application, *RSC Adv.*, 2013, **3**(43), 19789.

32 A. A. Umar, *et al.*, Poriferous microtablet of anatase TiO₂ growth on an ITO surface for high-efficiency dye-sensitized solar cells, *Sol. Energy Mater. Sol. Cells*, 2014, **122**, 174–182.

33 D. Dahlan, *et al.*, Synthesis of two-dimensional nanowall of Cu-Doped TiO₂ and its application as photoanode in DSSCs, *Phys. E*, 2017, **91**, 185–189.

34 A. A. Umar, *et al.*, Preparation of grass-like TiO₂ nanostructure thin films: effect of growth temperature, *Appl. Surf. Sci.*, 2013, **270**, 109–114.

35 D. Dahlan, *et al.*, Thermal impact on (001) faceted anatase TiO₂ microtablets and nanowalls's lattices and its effect on the photon to current conversion efficiency, *J. Phys. Chem. Solids*, 2019, **127**, 213–223.

36 A. Ali Umar, *et al.*, Poriferous microtablet of anatase TiO₂ growth on an ITO surface for high-efficiency dye-sensitized solar cells, *Sol. Energy Mater. Sol. Cells*, 2014, **122**, 174–182.

37 A. A. Shah, A. A. Umar and M. M. Salleh, Porous (001)-faceted anatase TiO₂ nanorice thin film for efficient dye-sensitized solar cell, *EPJ Photovoltaics*, 2016, **7**, 70501.

38 A. A. Umar, *et al.*, Preparation of grass-like TiO₂ nanostructure thin films: effect of growth temperature, *Appl. Surf. Sci.*, 2013, **270**, 109–114.

39 A. Ali Umar and M. Oyama, Synthesis of Palladium Nanobricks with Atomic-Step Defects, *Cryst. Growth Des.*, 2008, **8**(6), 1808–1811.

40 J. Zhang, *et al.*, PdPt bimetallic nanoparticles enabled by shape control with halide ions and their enhanced catalytic activities, *Nanoscale*, 2016, **8**(7), 3962–3972.

41 W. Hong, *et al.*, Bimetallic PdPt nanowire networks with enhanced electrocatalytic activity for ethylene glycol and glycerol oxidation, *Energy Environ. Sci.*, 2015, **8**(10), 2910–2915.

42 A. Bhukta, *et al.*, Growth of large aspect ratio AuAg bimetallic nanowires on Si(110) substrate, *Appl. Surf. Sci.*, 2017, **407**, 337–344.

43 N. F. Sulaiman, W. A. W. A. Bakar and R. Ali, Response surface methodology for the optimum production of biodiesel over $Cr/Ca/\gamma-Al_2O_3$ catalyst: catalytic performance and physico-chemical studies, *Renewable Energy*, 2017, **113**, 697–705.

44 C.-T. Li, *et al.*, A composite film of TiS_2/PEDOT:PSS as the electrocatalyst for the counter electrode in dye-sensitized solar cells, *J. Mater. Chem. A*, 2013, **1**(47), 14888–14896.

45 I. Yang, *et al.*, Relationships between pore size and charge transfer resistance of carbon aerogels for organic electric double-layer capacitor electrodes, *Electrochim. Acta*, 2017, **223**, 21–30.

46 Q. Tang, *et al.*, Dissolution Engineering of Platinum Alloy Counter Electrodes in Dye-Sensitized Solar Cells, *Angew. Chem., Int. Ed.*, 2015, **54**(39), 11448–11452.

47 A. A. Shah, A. A. Umar and M. M. Salleh, Efficient quantum capacitance enhancement in DSSC by gold nanoparticles plasmonic effect, *Electrochim. Acta*, 2016, **195**, 134–142.

48 P. Yang and Q. Tang, A branching NiCuPt alloy counter electrode for high-efficiency dye-sensitized solar cell, *Appl. Surf. Sci.*, 2016, **362**, 28–34.

49 P. S. Gnanasekar, *et al.*, Pt-free, low-cost and efficient counter electrode with carbon wrapped $VO_2(M)$ nanofiber for dye-sensitized solar cells, *Sci. Rep.*, 2019, **9**, 5177–5188.

50 J. Theerthagiri, *et al.*, One-step electrochemical deposition of $Ni_{1-x}Mo_xS$ ternary sulfides as an efficient counter electrode for dye-sensitized solar cells, *J. Mater. Chem. A*, 2016, **4**(41), 16119–16127.

51 W. Wang, *et al.*, $FeSe_2$ films with controllable morphologies as efficient counter electrodes for dye-sensitized solar cells, *Chem. Commun.*, 2014, **50**(20), 2618–2620.

52 X. Zuo, *et al.*, NiS nanoparticles anchored on reduced graphene oxide to enhance the performance of dye-sensitized solar cells, *J. Mater. Sci.: Mater. Electron.*, 2015, **26**(10), 8176–8181.

53 Y. Zhou, *et al.*, Enhanced dye-sensitized solar cells performance using anatase TiO_2 mesocrystals with the Wulff construction of nearly 100% exposed {101} facets as effective light scattering layer, *Dalton Trans.*, 2014, **43**(12), 4711–4719.

Karya#4 Plagiasi

1 repository.bilkent.edu.tr
Internet Source
3%

2 search.ndltd.org
Internet Source
2%

3 Altaf Yahya Ahmed Al-She'irey, Siti Khatijah Md Saad, Akrajas Ali Umar, Mohd Yusri Abd Rahman, Muhamad Mat Salleh. "(001) faceted-Ga-TiO2 microtablet synthesis and its organic perovskite sensitized solar cells characterization", Journal of Alloys and Compounds, 2016
Publication
1%

4 Akrajas Ali Umar, Siti Khatijah Md Saad, Marjoni Imamora Ali Umar, Mohd Yusri Abd Rahman, Munetaka Oyama. "Advances in porous and high-energy (001)-faceted anatase TiO 2 nanostructures", Optical Materials, 2018
Publication
1%

5 Muniyandi Bagavathi, Alagar Ramar, Ramiah Saraswathi. "Fe 3 O 4 –carbon black
1%

nanocomposite as a highly efficient counter electrode material for dye-sensitized solar cell", Ceramics International, 2016
Publication

6   Aamna Balouch, Akrajas Ali Umar, Athar Ali Shah, Muhamad Mat Salleh, Munetaka Oyama. "Efficient Heterogeneous Catalytic Hydrogenation of Acetone to Isopropanol on Semihollow and Porous Palladium Nanocatalyst", ACS Applied Materials & Interfaces, 2013
Publication
1%

7   Saad, Siti Khatijah Md, Akrajas Ali Umar, Mohd. Yusri Abd. Rahman, and Muhamad Mat Salleh. "Porous Zn-doped TiO2 nanowall photoanode: Effect of Zn2+ concentration on the dye-sensitized solar cell performance", Applied Surface Science, 2015.
Publication
1%

8   Muhammad Nurdin, Maulidiyah Maulidiyah, La Ode Agus Salim, Muhammad Zakir Muzakkar, Akrajas Ali Umar. "High performance cypermethrin pesticide detection using anatase TiO2-carbon paste nanocomposites electrode", Microchemical Journal, 2019
Publication
1%